PAPER • OPEN ACCESS

Density compensated diodes for small field dosimetry: comprehensive testing and implications for design

To cite this article: Georgios Georgiou *et al* 2020 *Phys. Med. Biol.* **65** 155011

IOP Publishing Phys. Med. Biol. 65 (2020) 155011 https://doi.org/10.1088/1361-6560/ab91d9

Physics in Medicine & Biology

IPEM Institute of Physics and Engineering in Medicine

Density compensated diodes for small field dosimetry: comprehensive testing and implications for design

Georgios Georgiou[1,2,3], **Sudhir Kumar**[4,5], **Jan U Würfel**[6], **Tracy S A Underwood**[7], **James M Thompson**[8], **Mark A Hill**[8], **Carl G Rowbottom**[2,3] **and John D Fenwick**[1,2]

[1] Department of Molecular and Clinical Cancer Medicine, Institute of Translational Medicine, University of Liverpool, The Sherrington Building, Ashton Street, Liverpool L69 3BX, United Kingdom
[2] Department of Physics, Clatterbridge Cancer Centre, Clatterbridge Road, Wirral CH63 4JY, United Kingdom
[3] Department of Physics, University of Liverpool, Oliver Lodge Laboratory, Oxford Street, Liverpool L69 7ZE, United Kingdom
[4] Department of Radiation Oncology, Henry Ford Health System, 2799 W. Grand Boulevard, Detroit, MI 48202, United States of America
[5] Radiological Physics and Advisory Division, Bhabha Atomic Research Centre, CT & CRS Building, Anushaktinagar Mumbai-400094, India
[6] PTW-Freiburg, Loerracher Str. 7, 79115, Freiburg, Germany
[7] Division of Cancer Sciences, School of Medical Sciences, Faculty of Biology, Medicine & Health, The University of Manchester, Manchester M20 4BX, United Kingdom
[8] CRUK/MRC Oxford Institute for Radiation Oncology, University of Oxford, Gray Laboratories, ORCRB Roosevelt Drive, Oxford OX3 7DQ, United Kingdom

E-mail: geogeorgph@gmail.com

Keywords: small field, dosimetry, diode, detector response, density compensation

OPEN ACCESS

RECEIVED
9 March 2020

REVISED
24 April 2020

ACCEPTED FOR PUBLICATION
11 May 2020

PUBLISHED
31 July 2020

Abstract

Purpose. In small megavoltage photon fields, the accuracies of an unmodified PTW 60017-type diode dosimeter and six diodes modified by adding airgaps of thickness 0.6–1.6 mm and diameter 3.6 mm have been comprehensively characterized experimentally and computationally. The optimally thick airgap for density compensation was determined, and detectors were micro-CT imaged to investigate differences between experimentally measured radiation responses and those predicted computationally. *Methods*. Detectors were tested on- and off-axis, at 5 and 15 cm depths in 6 and 15 MV fields $\geq 0.5 \times 0.5$ cm^2. Computational studies were carried out using the EGSnrc/BEAMnrc Monte Carlo radiation transport code. Experimentally, radiation was delivered using a Varian TrueBeam linac and doses absorbed by water were measured using Gafchromic EBT3 film and ionization chambers, and compared with diode readings. Detector response was characterized via the $k_{Q_{clin},Q_{msr}}^{f_{clin},f_{msr}}$ formalism, choosing a 4×4 cm^2 reference field. *Results*. For the unmodified 60017 diode, the maximum error in small field doses obtained from diode readings uncorrected by $k_{Q_{clin},Q_{msr}}^{f_{clin},f_{msr}}$ factors was determined as 11.9% computationally at +0.25 mm off-axis and 5 cm depth in a 15 MV 0.5×0.5 cm^2 field, and 11.7% experimentally at −0.30 mm off-axis and 5 cm depth in the same field. A detector modified to include a 1.6 mm thick airgap performed best, with maximum computationally and experimentally determined errors of 2.2% and 4.1%. The 1.6 mm airgap deepened the modified dosimeter's effective point of measurement by 0.5 mm. For some detectors significant differences existed between responses in small fields determined computationally and experimentally, micro-CT imaging indicating that these differences were due to within-tolerance variations in the thickness of an epoxy resin layer. *Conclusions*. The dosimetric performance of a 60017 diode detector was comprehensively improved throughout 6 and 15 MV small photon fields via density compensation. For this approach to work well with good detector-to-detector reproducibility, tolerances on dense component dimensions should be reduced to limit associated variations of response in small fields, or these components should be modified to have more water-like densities.

1. Introduction

Radiation doses absorbed by water from small non-equilibrium megavoltage photon fields should ideally be measured using detectors with effective atomic numbers and densities sufficiently close to water to limit spectral and lateral electronic disequilibrium effects, and sensitive volumes small enough to minimize volume averaging (IAEA 2017). Silicon diodes meet two of these criteria since their sensitive volumes are typically 1 mm^2 in cross-section, and the atomic number of silicon is close enough to water to limit spectral effects in small fields, particularly relative to 4 × 4 cm^2 rather than 10 × 10 cm^2 reference fields. The density of silicon is 2.33 g cm^{-3}, though, and compared to unit density water this causes diodes to over-read in small fields relative to wider fields (Scott *et al* 2012, Bassinet *et al* 2013, Underwood *et al* 2013a, Charles *et al* 2014, Fenwick *et al* 2018).

This problem can be overcome by offsetting the non-unit density materials with additional materials of contrasting density ('density compensation', Underwood *et al* 2012, 2013b). For example, several studies have demonstrated that errors in small field dose measurements made directly from diode detector readings, without applying field-size-specific corrections, can be reduced by adding air cavities to the diodes (Charles *et al* 2013, 2014, Underwood *et al* 2015b).

Underwood *et al* (2015b) characterized a set of density compensated dosimeters which PTW-Freiburg (Freiburg, Germany) manufactured by building spacer-rings into 60017-type unshielded diode detectors, creating airgaps of different thicknesses. The detectors were tested experimentally in a 6 MV photon beam, comparing diode readings with doses measured using Gafchromic EBT3 film (Ashland Inc, Covington, Kentucky), and were further characterized computationally via Monte Carlo radiation transport calculations. Data from both approaches showed that the maximum error in uncorrected dose measurements made on-axis at 5 cm depth in fields ≥0.5 × 0.5 cm^2 was 8% for an unmodified 60017 detector calibrated in a 10 × 10 cm^2 field, but fell to <2% for a detector with a 1.0 mm thick, 4.7 mm diameter airgap. The maximum error in uncorrected dose measurements made off-axis at 5 cm depth in the 6 MV 0.5 × 0.5 cm^2 field was also <2% of the on-axis dose-level for the modified detector. And according to further Monte Carlo calculations, errors in uncorrected dose measurements made on-axis at 5 cm depth in a 15 MV beam are also expected to be <2% for this detector.

Subsequently PTW-Freiburg built a new set of density compensated detectors based on the 60017 diode, with narrower 3.6 mm diameter airgaps molded directly into their plastic caps, removing the need to include spacer rings. Here we report results from our comprehensive testing of these new detectors, seeking to establish whether density compensation works only under restricted circumstances such as a narrow range of beam energies or depths, or with good generality throughout typical megavoltage photon beams used in radiotherapy. Specifically, we have tested detector response in 6 and 15 MV beams, on-axis at depths ranging from 0 to ≥27 cm and off-axis at 5 and 15 cm depths, using both experimental and computational methods. Spectral effects were minimized by using a reference field of 4 × 4 cm^2.

Throughout the study, detector response has been characterized via the $k^{f_{clin},f_{msr}}_{Q_{clin},Q_{msr}}$ formalism proposed by Alfonso (*et al* 2008) and further developed in the IAEA code of practice for small field dosimetry (2017). In this formalism, the measured dose-to-water in a clinical field f_{clin} of quality Q_{clin} is calculated as

$$\left(D_{w-point}\right)^{f_{clin}}_{Q_{clin}} = M^{f_{clin}}_{Q_{clin}} N^{f_{msr}}_{Q_{msr}} k^{f_{clin},f_{msr}}_{Q_{clin},Q_{msr}} \quad (1)$$

where M is the reading of a detector placed at the measurement point in water and irradiated using the clinical field, and N is the absorbed dose-to-water calibration coefficient obtained for the detector placed on-axis in a machine-specific reference field f_{msr} of quality Q_{msr} at a standard depth in water, chosen here to be 5 cm. The correction factor $k^{f_{clin},f_{msr}}_{Q_{clin},Q_{msr}}$ accounts for any difference in detector response at the measurement points in the clinical and reference fields, and is given by the ratio of doses absorbed by water at the measurement points in these fields, divided by the ratio of readings from the detector when located at the same points.

$$k^{f_{clin},f_{msr}}_{Q_{clin},Q_{msr}} = \left[\frac{\left(D_{w-point}\right)^{f_{clin}}_{Q_{clin}} / M^{f_{clin}}_{Q_{clin}}}{\left(D_{w-point}\right)^{f_{msr}}_{Q_{msr}} / M^{f_{msr}}_{Q_{msr}}}\right] \quad (2)$$

We have determined $k^{f_{clin},f_{msr}}_{Q_{clin},Q_{msr}}$ factors experimentally and via Monte Carlo calculations carried out for detector models built in software according to the manufacturer's blueprints. To check for any discrepancies between the blueprints and the geometries of the real diode detectors tested experimentally, the detectors were imaged using a micro-CT scanner.

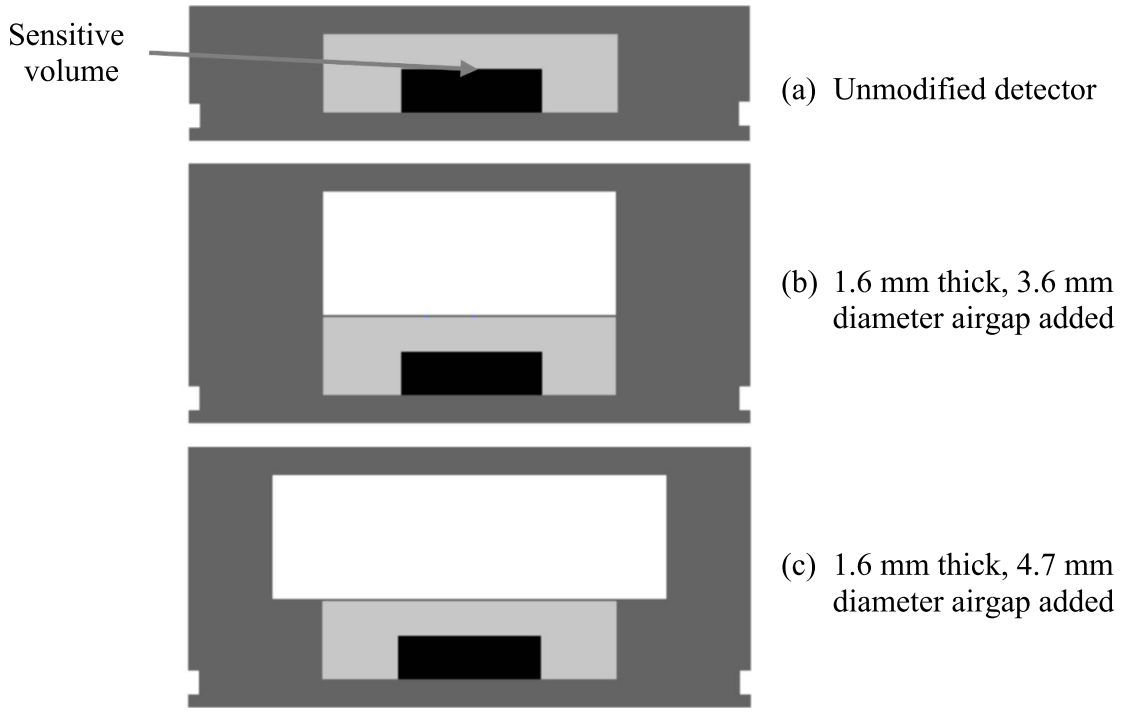

Figure 1. Schematic representations of the PTW 60017 diode detector: (a) unmodified; (b) modified to include a 1.6 mm thick, 3.6 mm diameter airgap; (c) with a 1.6 mm thick, 4.7 mm diameter airgap (not manufactured). Air is shown in white, the silicon cuboid in black and its epoxy housing in light grey. Other detector components are shown in dark grey, and most of the detector stem is omitted.

2. Methods

2.1. Detectors

An unmodified PTW 60017-type diode dosimeter was tested together with six other 60017 detectors modified to contain airgaps of diameter 3.6 mm and thicknesses 0.6, 0.8, 1.0, 1.2, 1.4 and 1.6 mm. The airgaps were built directly into the RW3 plastic caps of the detectors, rather than being created by adding a removable and adjustable cap to the detector top as proposed and tested by (Charles *et al* 2014). Progressively taller RW3 caps were used to accommodate thicker airgaps, but the thickness of RW3 lying above the airgaps was held constant.

The sensitive volume of each detector is a thin disc of silicon with a cross-sectional area of 1 mm^2 and thickness of 30 μm (PTW 2018), its short-axis aligned with the detector long-axis. The disc lies at the upper surface of a wider and thicker cuboidal slab of silicon, which in turn is located within an epoxy resin housing located immediately below the RW3 detector cap and any airgap within it (figure 1). In unmodified 60017 diodes the effective point of measurement (EPOM) lies on the detector axis, at 1.33 mm below the top surface of the detector according to the manufacturer's specification. This point differs slightly from the centre of the detector's sensitive volume because the materials overlying the sensitive volume are not water-equivalent. The EPOM may vary in detectors containing airgaps, an issue we have studied by comparing percentage-depth-doses (PDDs) measured using unmodified and modified detectors.

When determining $k_{Q_{clin},Q_{msr}}^{f_{clin},f_{msr}}$ values, the detector EPOM is often placed at the measurement point in water (IAEA 2017). However, we defined the measurement point as lying 1.33 mm below the tops of diode detectors when experimentally measuring $k_{Q_{clin},Q_{msr}}^{f_{clin},f_{msr}}$, meaning that the EPOM and measurement point were coincident for the unmodified 60017 detector, but not necessarily for modified detectors. The effect of any EPOM offset will be negligible, though, because readings made in two fields appear as ratios in the $k_{Q_{clin},Q_{msr}}^{f_{clin},f_{msr}}$ factor, cancelling any slight redefinition of measurement depth. In computational determinations of $k_{Q_{clin},Q_{msr}}^{f_{clin},f_{msr}}$ we placed the centre of the sensitive volume at the measurement point, and this too will have negligible effect on the factors calculated.

To characterize how detector response varies with airgap diameter as well as thickness, particularly any difference between the 3.6 mm diameter airgaps investigated here and the 4.7 mm diameter gaps studied by Underwood *et al* (2015b), we have run radiation transport calculations for 60017-type detectors with

fictitious 4.7 and 5.6 mm diameter airgaps molded into the RW3 detector caps (figure 1), as well as the 3.6 mm wide airgaps built into detectors in practice.

2.2. Monte Carlo radiation transport calculations

Monte Carlo calculations were carried out using the EGSnrc system (Kawrakow *et al* 2011) run on a 64 core AMD 6378 Opteron-based computer. Phase-space files were created for fields of size 0.5×0.5 cm^2 and 4×4 cm^2 projected to isocentre, defined by the linear accelerator (linac) jaws. The files were generated using BEAMnrc (Rogers *et al* 2011a), running 6 and 15 MV beam models built and validated for Clinac iX and 2100 C treatment machines (Varian Medical Systems, Palo Alto, California) by Underwood *et al* (2013a) and Scott *et al* (2008) respectively, and setting the electron and photon cut-off parameters ECUT and PCUT to 700 and 10 keV.

Doses absorbed from these fields by water voxels located within a $50 \times 50 \times 50$ cm^3 water phantom were calculated using the DOSXYZnrc user-code (Rogers *et al* 2011b), selecting the PRESTA-II electron transport and exact boundary crossing algorithms, and setting ECUT and PCUT to 521 and 1 keV. Rayleigh scattering, binding effects in Compton interactions, relativistic spin effects in electron multiple scattering, and atomic relaxation events were modelled. Photon interaction cross-sections were taken from the XCOM database (Berger *et al* 2010), and photon energies in bremsstrahlung events were sampled using NIST database cross-sections (Hubbell and Seltzer 2004).

For the 6 and 15 MV beams, on-axis doses in water were calculated at 5 and 15 cm depths in the 0.5×0.5 cm^2 and 4×4 cm^2 fields, with the water tank positioned at 100 cm source-surface-distance (SSD). Off-axis dose-profiles were also calculated at these depths in the 0.5×0.5 cm^2 field, together with percentage depth-doses (PDDs) down the field's central axis. Average doses within voxels were used to approximate the point doses at their centres, and voxel dimensions were chosen to provide adequate spatial resolution while allowing doses to be computed with good statistical precision in reasonable times. Specifically, for the 0.5×0.5 cm^2 field on-axis doses and cross-profiles at 5 and 15 cm deep were calculated with a precision of $\leq \pm 0.5\%$ (2 standard deviations, s.d.) on-axis, and $\pm 1\%$ up to 1 mm beyond the field edge, using voxels of lateral dimensions 0.25×0.25 mm^2 and thickness 0.5 mm. PDDs were calculated using $0.25 \times 0.25 \times 1$ mm^3 voxels up to 5 cm depth and $0.25 \times 0.25 \times 10$ mm^3 voxels at greater depths, achieving a dose precision of $\leq \pm 0.5\%$, the coarser grid reflecting the greater range over which PDDs were calculated. For the 4×4 cm^2 field on-axis doses were calculated in wider $2 \times 2 \times 0.5$ mm^3 voxels, since dose-profiles at the field centre were quite flat, and a dose precision of $\pm 0.3\%$ was achieved.

To computationally characterize detector response, doses absorbed by detector sensitive volumes were calculated and used as simulated detector readings. Detector models were built from the manufacturer's blueprints using the EGS++ geometry package within the egs_chamber code (Wulff *et al* 2008). PEGS4 data-files containing cross-section and stopping-power data for detectors' constituent materials were generated using EGSnrcMP (Kawrakow *et al* 2006, 2011), setting AE and AP thresholds to 512 and 1 keV. To apply polarization effect corrections, the 'ICRU density correction' option was selected. For some materials polarization effect data was unavailable in EGSnrc, and corrections were instead generated using data from the NIST website (National Institute of Science and Technology 2018).

In-silico, the detector models were positioned within the water phantom, aligned parallel to the radiation beam. Doses in detector sensitive volumes were calculated using egs_chamber, setting ECUT and PCUT to 521 and 1 keV, and employing photon cross-section enhancement variance reduction with an enhancement factor of 128 inside a shell extending 2 cm beyond the sensitive volume (Wulff *et al* 2008).

On-axis detector sensitive volume doses were calculated to a precision of $\pm$ 0.2%, with the centres of sensitive volumes located at 5 and 15 cm depths in 0.5×0.5 cm^2 and 4×4 cm^2 fields. Simulations of PDD curves that would be measured for the 0.5×0.5 cm^2 field using diode detectors were made by computing doses in detector sensitive volumes positioned at depths increasing in 1 mm steps from 0 to 5 cm, in 1 cm steps up to 20 cm deep, and 5 cm steps to 35 cm deep. These doses were calculated to a precision of $\leq \pm 0.7\%$ up to 15 cm deep, and $\pm$ 1% beyond this. Off-axis profiles measured by detectors were simulated at 5 and 15 cm depths in the 0.5×0.5 cm^2 field, calculating sensitive volume doses for detector positions stepped across the field in 0.25 mm increments. Only half-profiles were computed since the beam and detector models were symmetric, and the precision of dose calculation was $\pm$ 0.7% at 1 mm beyond the field-edge. All computed doses were normalized by the numbers of electrons incident on the linac target.

Simulated $k^{f_{clin},f_{msr}}_{Q_{clin},Q_{msr}}$ factors and associated uncertainties were calculated from Monte Carlo doses and their uncertainties in water and detector sensitive volumes using equation (2). On-axis, at 5 cm depth in a 6 MV beam $k^{0.5,4\text{ cm}}_{Q_{0.5,\,4\text{ cm}}}$ factors were determined for all modelled detectors. Off-axis, or at 15 cm depth, or in the 15 MV beam $k^{0.5,4\text{ cm}}_{Q_{0.5,\,4\text{ cm}}}$ factors were computed only for the unmodified detector and for the modified detector

that performed best on-axis at 5 cm depth in the 6 MV beam. Likewise, 0.5 × 0.5 cm^2 field PDD curves obtained from diode measurements were simulated only for these two detectors.

2.3. Experimental measurements

A Varian TrueBeam linac oriented at 0° gantry angle delivered 6 and 15 MV photon beams to a Blue Phantom 2 water tank (IBA Dosimetry, Schwarzenbruck, Germany) positioned at 100 cm SSD. Doses were measured using diode detectors placed in the tank, aligned parallel to the beam-axis and connected to an electrometer box and associated OmniPro-Accept 7.4 computer software with no bias voltage. The detectors were set up so that their depths as reported by the water tank software lay 1.33 mm below their top surfaces.

Square fields of widths 0.5, 0.7, 1.0, 3.0, 4.0, 6.0 and 10.0 cm were measured at both beam energies, and a 1.5 cm field was also measured at 6 MV. The fields were defined by the linac jaws, with the MLCs fully retracted. Jaw settings described locations of 50% field-edges projected to isocentre, and once set they were maintained until measurements of the field using all detectors were complete.

For each field and detector, in-line and cross-line profiles were measured at 5 and 15 cm depths, and detector centering was adjusted if measured profile centres were offset by >0.3 mm from the initial origin. Readings were then taken with diode detectors positioned on-axis at 5 and 15 cm depths and irradiated using fixed numbers of monitor units (MUs). PDDs were also measured using the different detectors. Additional PDD data was obtained for the 4 × 4 cm^2 reference field, using a PTW 31010-type Semiflex ionization chamber with the central axis of its 0.125 cc sensitive volume aligned perpendicular to the beam axis, the measurement depth being identified as the depth of the chamber's EPOM, 1.6 mm above the central axis.

$k_{Q_{clin},\,4\,cm}^{f_{clin},4\,cm}$ factors were calculated from ratios of each detector's readings-per-MU in the clinical and 4 × 4 cm^2 reference fields, and corresponding ratios of doses in water measured using EBT3 film for fields $\leq$1.5 × 1.5 cm^2 and for the reference field, and using an IBA CC13 ionization chamber for fields $\geq$ 3 × 3 cm^2. Off-axis detector readings-per-MU and in-water doses-per-MU were obtained by multiplying on-axis detector and film readings by off-axis profiles. Uncertainties on $k_{Q_{clin},\,4\,cm}^{f_{clin},4\,cm}$ factors were calculated from underlying uncertainties on detector and film measurements, determined from repeat readings.

2.4. Radiochromic film techniques

Doses absorbed by water from small fields were measured using Gafchromic EBT3 film. Due to this film's near water-equivalent atomic number and density, its response varies little between small fields and wider fields in which it can be cross-calibrated against well-characterized detectors (Bassinet *et al* 2013, Underwood *et al* 2015b, Morales *et al* 2016, Fenwick *et al* 2018).

Measurements were made using 6 × 6 cm^2 film-squares cut from larger EBT3 sheets. The films were handled using nitrile gloves, and exposure to light and dust was minimized. Film-squares were placed one-by-one in a metallic frame, which gripped their edges and was fitted to the movement mechanism of the water tank holding the films horizontal when submerged in water (Underwood *et al* 2015b). Marks made on the film-squares before cutting them were used to ensure consistent film orientation.

To generate 6 and 15 MV calibration curves, five calibration film-squares were irradiated in a 4 × 4 cm^2 field at 5 cm depth in water, at each of seven known dose-levels between 0 and 4.35 Gy and for both beam energies. Doses in other fields were then measured using film-squares positioned at depths of 5 and 15 cm in water. For each field-size and depth combination three to five films were irradiated, scaling MUs so that around 2 Gy was delivered to every film-square.

Films were scanned 48 h after irradiation using an Epson V750 Pro scanner (Epson UK, Hemel Hempstead). To ensure consistency of processing (Micke *et al* 2011, Lewis *et al* 2012, Papaconstadopoulos *et al* 2014) the film-squares were placed on the scanner at a fixed position and scanned using a standard protocol (professional mode, 48-bit colour with 150 dots-per-inch, DPI), saving scans as uncompressed TIFF files with no corrections or filters applied.

Using in-house software (Underwood *et al* 2015b) calibration curves were generated from scanned calibration films, and dose-maps were extracted from scans of other films via the triple-channel method (Micke *et al* 2011, Lewis *et al* 2012). The software returns a grid of doses, each point representing the average dose in a group of 3 × 3 scan pixels having a total area of 0.51 × 0.51 mm^2. Measured on-axis doses-per-MU and off-axis dose-profiles were calculated as averages of values obtained from all films irradiated at the depth and field-size of interest.

2.5. Imaging of detectors

Micro-CT imaging of the diode detectors was performed using a VECTor^{4}CT system (MILabs, Utrecht, The Netherlands). Images were acquired at 55 kV and 0.19 mA with detectors positioned along the central axis of the scanner.

Table 1. Monte Carlo 6 MV $k_{Q_{0.5,\,4\,cm}}^{0.5,4\,cm}$ factors calculated for 60017 diode detectors with airgaps of thickness 0.0–1.6 mm and diameter 3.6 mm (as manufactured), 4.7 mm and 5.6 mm. The detectors were positioned on-axis at 5 cm depth in water and irradiated in a 0.5 × 0.5 cm^2 clinical field at 100 cm SSD, the reference condition being on-axis 5 cm deep in a 4 × 4 cm^2 field. Uncertainties are ± 2 standard deviations (s.d.).

Airgap thickness (mm)	3.6 mm diameter airgap $k_{Q_{0.5,\,4\,cm}}^{0.5,\,4\,\mathbf{cm}}$	4.7 mm diameter airgap $k_{Q_{0.5,\,4\,cm}}^{0.5,\,4\,\mathbf{cm}}$	5.6 mm diameter airgap $k_{Q_{0.5,\,4\,cm}}^{0.5,\,4\,\mathbf{cm}}$
0.0 (unmodified 60017)	**0.910 ± 0.005**	—	—
0.6	0.941 ± 0.008	0.939 ± 0.009	0.945 ± 0.008
0.8	0.956 ± 0.008	0.957 ± 0.008	0.962 ± 0.008
1.0	0.969 ± 0.009	0.977 ± 0.009	0.976 ± 0.008
1.2	0.971 ± 0.008	0.987 ± 0.007	0.989 ± 0.008
1.4	0.979 ± 0.008	1.006 ± 0.006	1.011 ± 0.006
1.6	**0.995 ± 0.006**	1.017 ± 0.006	1.019 ± 0.008

Table 2. Monte Carlo 6 and 15 MV $k_{Q_{0.5,\,4\,cm}}^{0.5,4\,cm}$ correction factors calculated for an unmodified 60017 diode and a detector with a 1.6 mm thick, 3.6 mm diameter airgap, positioned on-axis at 5 and 15 cm depths in water, the reference condition being on-axis at 5 cm depth in a 4 × 4 cm^2 field. ± 2 s.d. confidence intervals are shown.

Airgap thickness (mm)	6 MV 5 cm deep $k_{Q_{0.5,\,4\,cm}}^{0.5,\,4\,\mathbf{cm}}$	6 MV 15 cm deep $k_{Q_{0.5,\,4\,cm}}^{0.5,\,4\,\mathbf{cm}}$	15 MV 5 cm deep $k_{Q_{0.5,\,4\,cm}}^{0.5,\,4\,\mathbf{cm}}$	15 MV 15 cm deep $k_{Q_{0.5,\,4\,cm}}^{0.5,\,4\,\mathbf{cm}}$
0.0 (unmodified 60017)	0.910 ± 0.005	0.913 ± 0.005	0.896 ± 0.005	0.900 ± 0.005
1.6	0.995 ± 0.006	0.997 ± 0.006	1.006 ± 0.006	1.003 ± 0.006

3. Results

3.1. Monte Carlo data

3.1.1. Simulated on-axis $k_{Q_{0.5,\,4\,cm}}^{0.5,\,4\,cm}$ factors

Computed $k_{Q_{0.5,\,4\,cm}}^{0.5,\,4\,cm}$ values are listed in table 1 for detectors positioned on-axis in a 6 MV 0.5 × 0.5 cm^2 field at 5 cm depth in water. The results show two patterns. Firstly, detector response was substantially improved by adding airgaps, $k_{Q_{0.5,\,4\,cm}}^{0.5,\,4\,cm}$ rising progressively towards unity with increasing airgap thickness from 0.910 ± 0.005 (2 s.d.) for the unmodified 60017-type detector to 0.995 ± 0.006 for a detector with an airgap of 1.6 mm thickness and 3.6 mm diameter. Secondly, for airgaps of thickness ≤ 1 mm, calculated $k_{Q_{0.5,\,4\,cm}}^{0.5,\,4\,cm}$ values did not vary significantly across the range of airgap diameters studied. For thicker airgaps, however, $k_{Q_{0.5,\,4\,cm}}^{0.5,\,4\,cm}$ rose significantly with increasing diameter, by 0.032 between diameters of 3.6 and 5.6 mm for a 1.4 mm thick airgap (p = 0.0014, 2-sided).

As shown in table 2, very similar $k_{Q_{0.5,\,4\,cm}}^{0.5,\,4\,cm}$ values were computed for the 6 MV beam when the unmodified detector and the detector with the 1.6 mm thick, 3.6 mm diameter airgap were placed on-axis at 15 rather than 5 cm depth in water in the 0.5 × 0.5 cm^2 field, the reference condition still being 5 cm deep in a 4 × 4 cm^2 field. Specifically, at 15 cm depth $k_{Q_{0.5,\,4\,cm}}^{0.5,\,4\,cm}$ was 0.913 ± 0.005 for the unmodified detector and 0.997 ± 0.006 for the detector with the airgap. On-axis $k_{Q_{0.5,\,4\,cm}}^{0.5,\,4\,cm}$ values calculated for these two detectors in a 15 MV beam are also shown in table 2. At this energy, $k_{Q_{0.5,\,4\,cm}}^{0.5,\,4\,cm}$ for the unmodified detector was roughly 0.90 at both 5 and 15 cm depths, while for the detector with the 1.6 mm airgap it was 1.006 ± 0.006 and 1.003 ± 0.006 at the two depths.

3.1.2. Simulated off-axis detector response

Figure 2 shows Monte Carlo simulated responses for the unmodified 60017 detector and the detector with the 1.6 mm thick, 3.6 mm diameter airgap, calculated at 5 cm depth in water across a 6 MV 0.5 × 0.5 cm^2 field in the direction of travel of the lower (X) jaws, which produce the sharpest penumbra. Computed in-water dose profiles are graphed alongside simulations of the profiles that would be measured by the two detectors, all normalized to on-axis values. Small, high density detectors like the 60017 diode over-estimate penumbra sharpness (Francescon *et al* 2014, Hartmann and Zink 2018), but as shown in figure 2 the effect is largely eliminated by the airgap. The variation of the $k_{Q_{0.5,\,4\,cm}}^{0.5,\,4\,cm}$ correction factor with position off-axis is also plotted in figure 2, the reference condition still being on-axis at 5 cm depth in a 4 × 4 cm^2 field.

In figure 3, simulated errors in the off-axis doses that would be measured at 5 and 15 cm depths without applying correction factors to readings from the same two detectors are graphed as fractions of on-axis dose, for the 6 and 15 MV beams. Detector response off-axis was substantially improved by adding the 1.6 mm

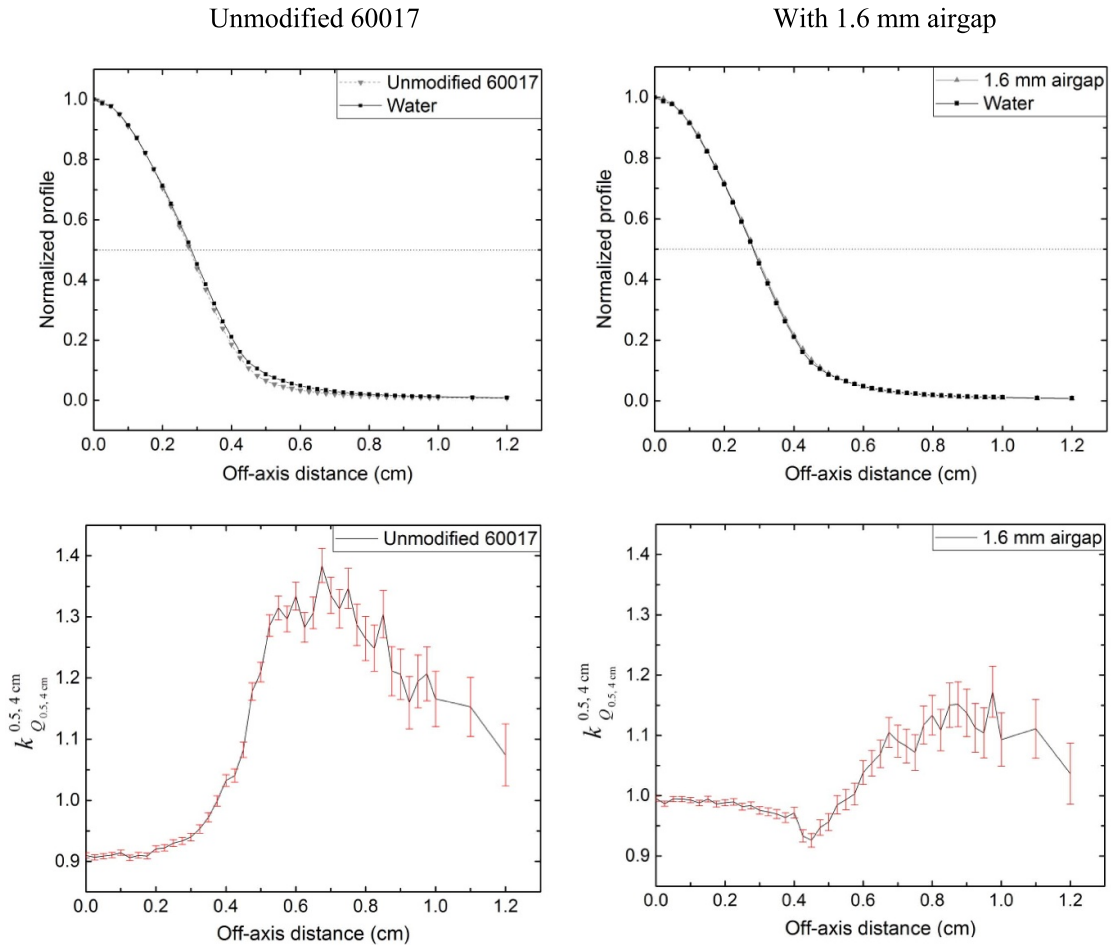

Figure 2. Monte Carlo calculations of response off-axis in a 6 MV 0.5 × 0.5 cm^2 field at 5 cm depth in water, for the unmodified 60017 detector and a detector with a 1.6 mm wide, 3.6 mm diameter airgap. Plots show simulated in-water and detector-measured profiles normalized to on-axis values (top), and k correction factors (bottom). Statistical uncertainties are ± 2 standard deviations (s.d.).

airgap, the maximum error for the modified detector being 1.3% ± 0.5% of the on-axis dose at 5 cm depth and 0.5% ± 0.5% of the on-axis dose at 15 cm depth in the 6 MV beam, and 2.2% ± 0.3% at both depths in the 15 MV beam.

3.1.3. Simulated depth-dose curves

PDDs computed for the 6 MV 0.5 × 0.5 cm^2 field are plotted in figure 4. Depth-dose data calculated in water is shown together with simulations of PDD curves that would be measured by the unmodified 60017 detector and the detector with the 1.6 mm thick, 3.6 mm diameter airgap. Statistical uncertainties on calculated doses are not plotted, but were 1% or less (2 s.d.).

In panel (a) of figure 4, measurement depths indicated for the unmodified detector correspond to the EPOM location, 1.33 mm below the detector's top surface. For the detector with the 1.6 mm thick airgap two curves are plotted, with measurement depths corresponding respectively to locations 1.33 mm and 1.78 mm below the detector's top surface. The latter build-up curve agrees well with the curves calculated in water and for the unmodified detector, indicating that the 1.6 mm airgap has increased the depth of the EPOM below the modified detector 's top surface by 0.45 mm.

In panels (b)–(c) of figure 4, measurement depths for the unmodified and modified detectors correspond respectively to locations 1.33 and 1.78 mm below their respective top surfaces, leading to good agreement between the in-water PDD and the PDDs simulated for the two detectors, both in the build-up region and at greater depths. Specifically, ratios of the simulated detector-measured and in-water PDDs, normalized to a value of one at 5 cm depth, differed from unity by a maximum of 1.3% between depths in water of 1 and 35 cm, comparable to the noise on the data.

In the 15 MV beam, the EPOM of the detector with the 1.6 mm thick airgap lay 1.87 mm below the detector's upper surface, little different to the EPOM at 6 MV.

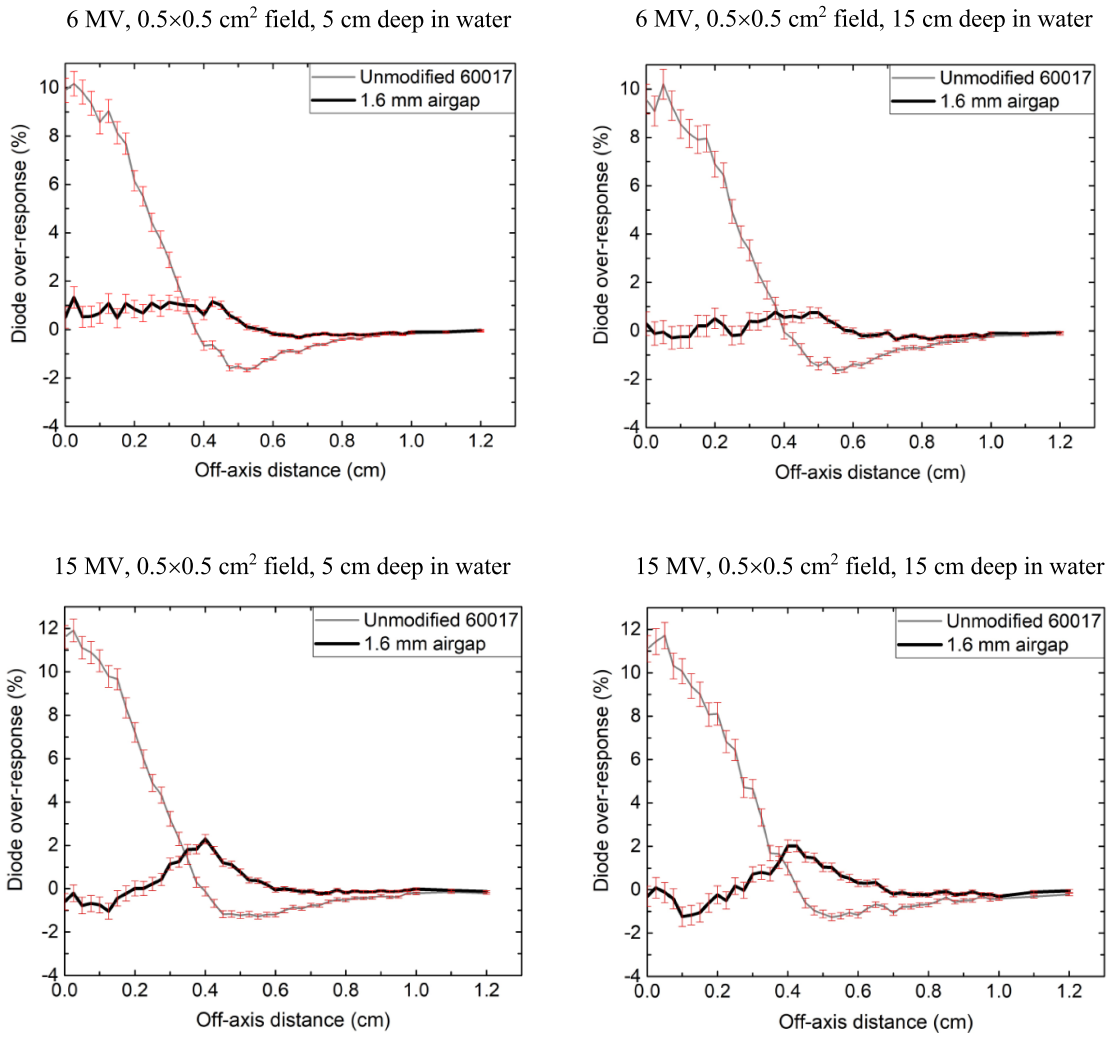

Figure 3. Monte Carlo calculations of errors in doses obtained from uncorrected detector readings off-axis in a 0.5 × 0.5 cm^2 field at 5 and 15 cm depths in water, normalized to on-axis doses, for an unmodified 60017 detector and for a detector with a 1.6 mm thick, 3.6 mm diameter airgap. ± 2 s.d. confidence intervals are shown.

3.2. Experimental data

3.2.1. Measured on-axis $k_{Q_{clin},4\,cm}^{f_{clin},4\,cm}$ factors

In figure 5 $k_{Q_{clin},4\,cm}^{f_{clin},4\,cm}$ factors determined experimentally on-axis in 6 and 15 MV beams at 5 and 15 cm depths in water are plotted against field-sizes from 0.5 × 0.5 to 10 × 10 cm^2. In the 6 MV beam the modified 60017 detector with a 1.6 mm airgap added performed best overall, with measured $k_{Q_{0.5,\,4\,cm}}^{0.5,\,4\,cm}$ values of 0.993 ± 0.013 and 1.007 ± 0.013 (2 s.d.) at 5 and 15 cm depths respectively, and $k_{Q_{clin},4\,cm}^{f_{clin},4\,cm}$ values lying within ±1% and ±2% of 1.00 for all the fields at these depths. The unmodified 60017 detector and a detector with a 1.4 mm airgap performed least well, with $k_{Q_{0.5,\,4\,cm}}^{0.5,\,4\,cm}$ values of 0.914 ± 0.011 and 1.040 ± 0.012 respectively at 5 cm depth in water, and 0.930 ± 0.007 and 1.054 ± 0.009 at 15 cm depth.

The detector with the 1.6 mm airgap also performed relatively well in the 15 MV beam, with $k_{Q_{0.5,\,4\,cm}}^{0.5,\,4\,cm}$ values of 1.018 ± 0.015 and 1.031 ± 0.019 at depths of 5 and 15 cm. And again, the unmodified detector and the detector with the 1.4 mm airgap performed least well, with $k_{Q_{0.5,\,4\,cm}}^{0.5,\,4\,cm}$ values of 0.904 ± 0.014 and 1.062 ± 0.016 respectively at 5 cm depth.

While the relatively good experimental performance of the detector with the 1.6 mm airgap and the poor performance of the unmodified detector agree with the overall pattern seen in the Monte Carlo calculations, some of the experimental results were unexpected. In particular, the measured $k_{Q_{0.5,\,4\,cm}}^{0.5,\,4\,cm}$ factors did not rise progressively with increasing airgap thickness, even after allowing for experimental uncertainties. For example, $k_{Q_{0.5,\,4\,cm}}^{0.5,\,4\,cm}$ values for detectors with 0.8 and 1.4 mm airgaps were expected to be lower than those for 1.0 and 1.6 mm airgap detectors respectively, but were significantly higher in practice. Reasons for these anomalies are explored in section 3.3.

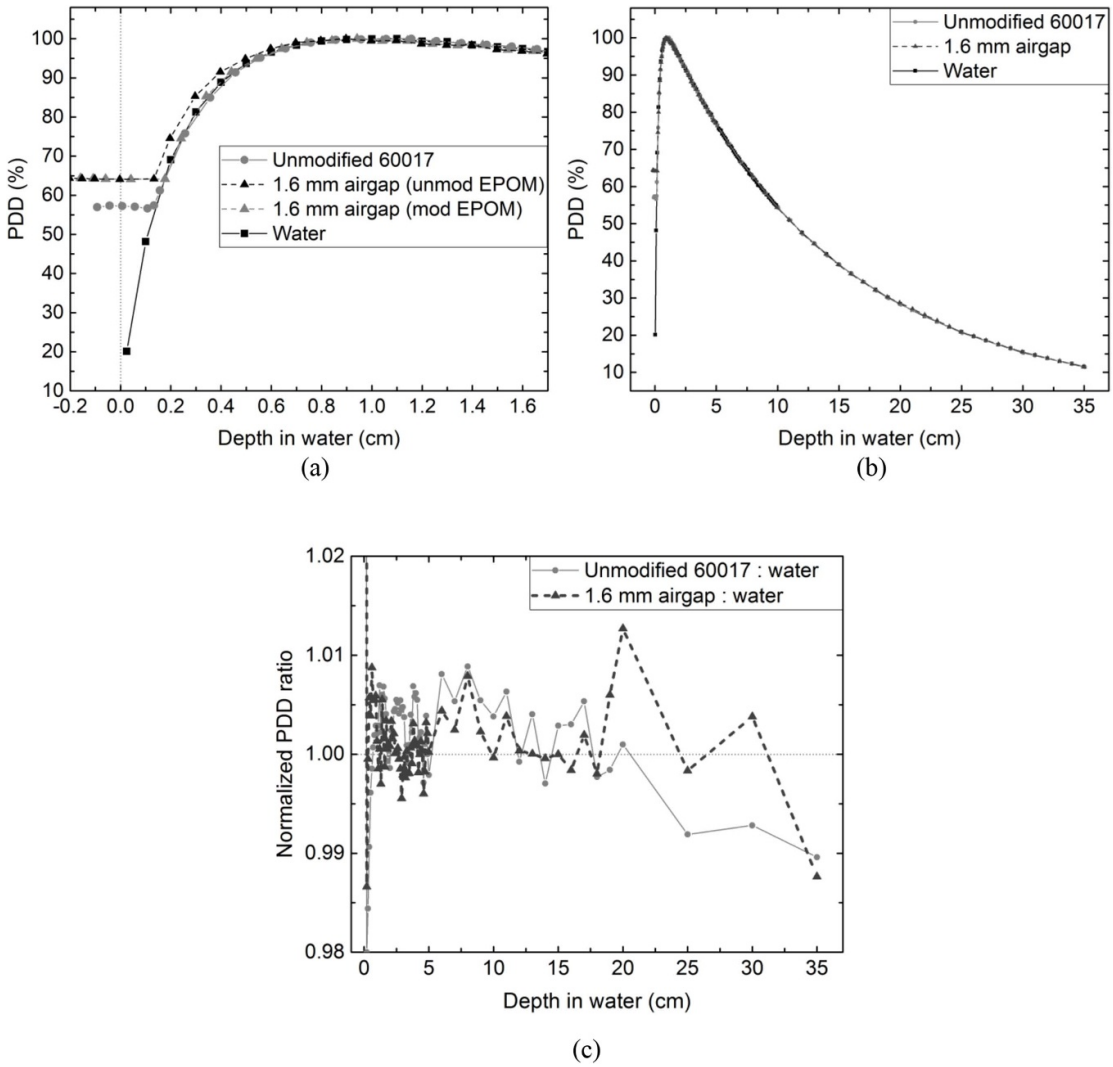

Figure 4. Monte Carlo PDD data for a 6 MV 0.5 × 0.5 cm^2 field, showing curves calculated in water, and simulations of PDDs measured by the unmodified 60017 detector and a detector with a 1.6 mm thick, 3.6 mm diameter airgap. The plots show: (a) build-up curves; (b) complete PDD curves; (c) ratios of PDD curves, calculated after correcting for effects of small differences in measurement points due to EPOM shifts via linear interpolation, and normalized to unity at 5 cm depth. Detector measurement depths were defined as: (a) 1.33 mm below the top of the unmodified detector, and 1.33 mm ('unmod EPOM') or 1.78 mm ('mod EPOM') below the top of the modified detector; (b), (c) 1.33 and 1.78 mm below the tops of the unmodified and modified detectors respectively.

3.2.2. Measured off-axis detector response

For the unmodified 60017 detector and the 1.6 mm airgap detector, errors in off-axis dose measurements across a 6 MV 0.5 × 0.5 cm^2 field resulting from using uncorrected detector readings are plotted in figure 6. The curves were calculated from diode and film data measured along the direction of travel of the lower (X) jaws, and are noisy due to the imprecise though accurate nature of film dosimetry, despite the film profiles having been averaged over the three films irradiated at each depth. Calculated confidence intervals are shown on-axis, at the field edge, and beyond the edge.

For the unmodified detector the maximum error was 9.7% of the on-axis dose. For the detector with the 1.6 mm airgap the maximum error was 3.5%, but this occurred at a spike in the plot consistent with the scale of noise in its vicinity, and the underlying error in detector response may well be $\leq$2% as indicated by the Monte Carlo results. Measurements for a 1.5 × 1.5 cm^2 field are also plotted in figure 6. Again, the airgap improved detector performance, although this wider field was less dosimetrically challenging, the maximum error being 3.6% for the unmodified detector and 2.4% for the detector with the airgap. In the 15 MV beam (data not shown) the maximum error at 5 or 15 cm depth in a 0.5 × 0.5 cm^2 field was 11.7% for the unmodified 60017 detector (at −0.3 mm off-axis, 5 cm depth), and 4.1% for the detector with the 1.6 mm airgap (at +0.4 mm off-axis, 15 cm depth).

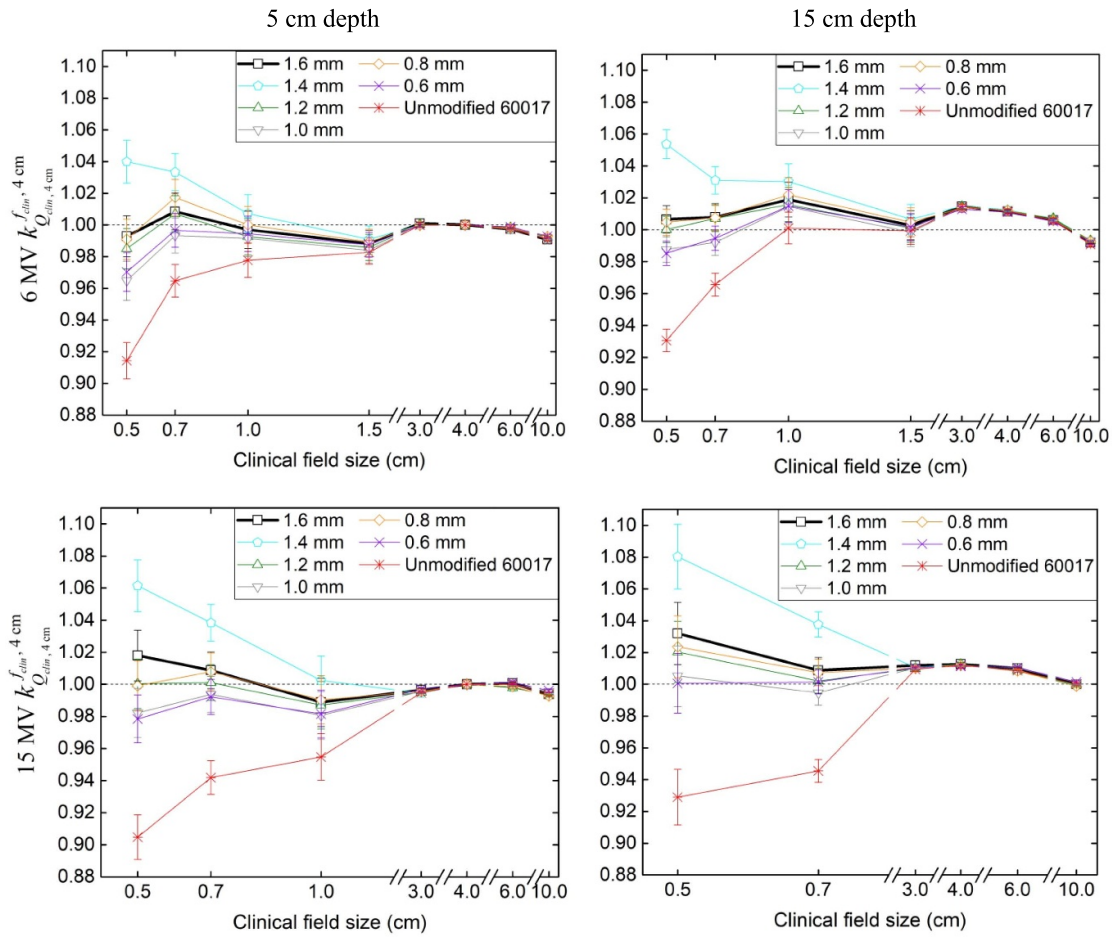

Figure 5. On-axis $k^{f_{clin},4\,cm}_{Q_{clin},4\,cm}$ values experimentally measured in 6 MV (top) and 15 MV (bottom) square fields at 5 cm (left) and 15 cm (right) depths in water for the unmodified 60017 detector and modified detectors with airgaps of 0.6–1.6 mm as indicated in the figure captions. The reference condition was on-axis in a 4 × 4 cm^2 field, at 5 cm depth in water. ± 2 s.d. confidence intervals are shown.

3.2.3. Measured depth-dose curves

Figure 7 shows depth-dose data measured for 6 MV 0.5 × 0.5 and 4 × 4 cm^2 fields using the diode detectors investigated. Figure 7(a) plots dose build-up curves measured for the 0.5 × 0.5 cm^2 field, shifted longitudinally so that their kick-points all lie at a measurement depth of 1.33 mm. A kick happens when the top of a detector has fallen just below the water surface and the amount of material overlying the sensitive volume begins to increase (Underwood *et al* 2015b). Consequently, for the unmodified 60017 detector the plotted measurement depth corresponds to the EPOM depth, while for modified detectors the longitudinal shifts visible in the figure between their depth-dose curves and the curve measured by the unmodified detector correspond to changes in their EPOM depths relative to the unmodified detector, only reversed in direction.

Table 3 lists changes in EPOM, determined from build-up curve shifts at the level of 80% of the PDD maximum, for 0.5 × 0.5, 1.5 × 1.5 cm^2 and 4 × 4 cm^2 fields. Although differences between EPOMs measured for any one detector in the different fields were relatively small, the maximum being 0.3 mm, differences in EPOMs between the detectors were greater, up to 0.9 mm. Similar to the on-axis $k^{0.5,\,4\,cm}_{Q_{0.5,\,4\,cm}}$ values, though, these EPOM differences did not increase progressively with airgap thickness.

For the 4 × 4 cm^2 field, PDDs measured by the diode detectors and the Semiflex ionization chamber are plotted over their full measured ranges in figure 7(b). The ratio of PDDs measured by the unmodified 60017 detector and the Semiflex chamber is plotted in figure 7(c), normalized to a value of one at 5 cm depth. The difference between the EPOMs of the detectors has been adjusted for in the plot, which shows a progressive fall in doses measured using the unmodified 60017 diode relative to those measured using the ionization chamber, by around 2% between depths of 5 and 27 cm, similar to a pattern observed by Underwood *et al* (2015a, 2015b). This progressive fall probably reflects a known trend for diode response to lessen as the dose-rate decreases (Jursinic 2013), rather than being due to spectral variation with depth, which would have created a similar but unobserved trend in the Monte Carlo data (figure 4). Also plotted in figure 7(c) is the

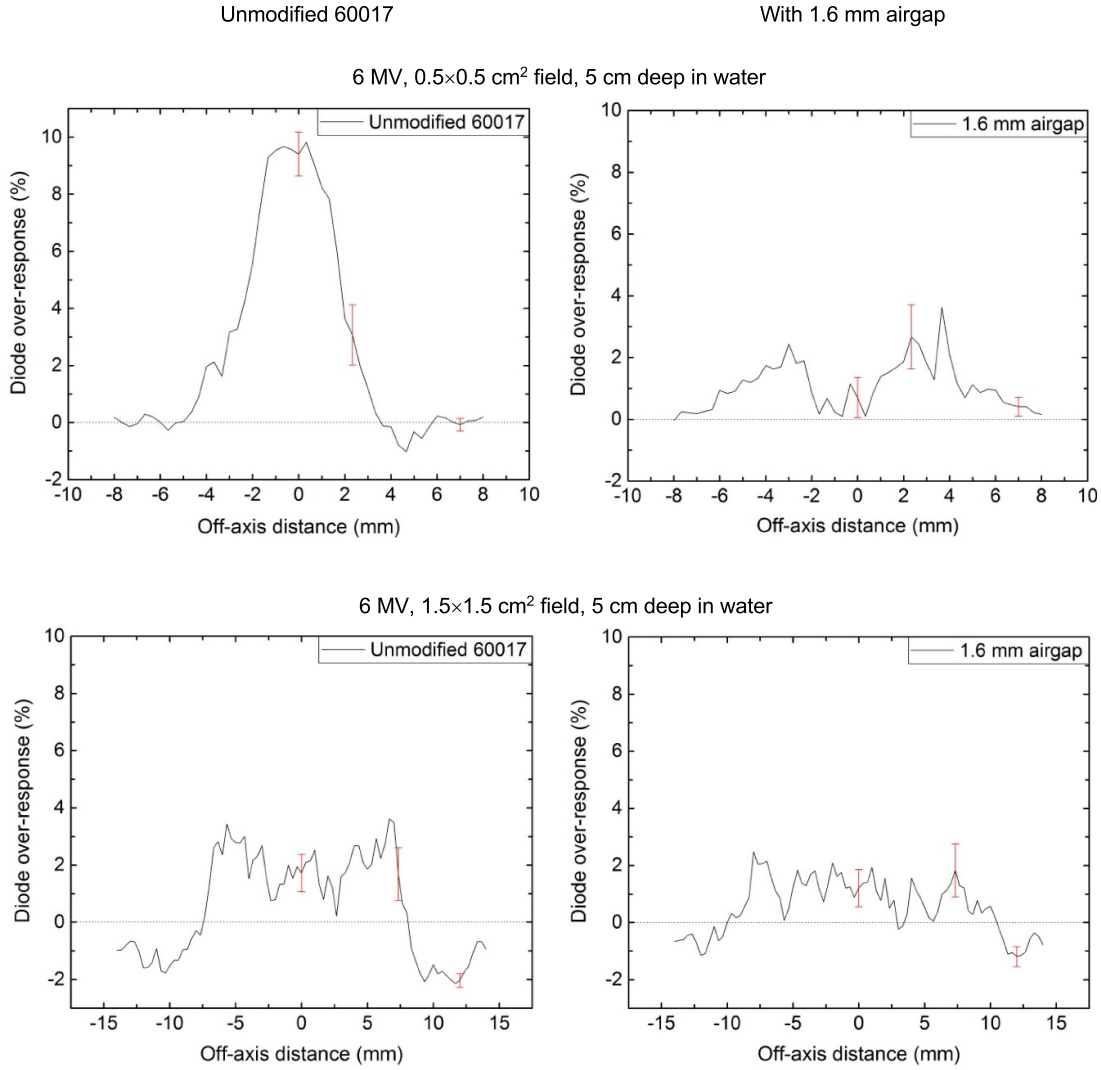

Figure 6. Off-axis responses experimentally measured in a 6 MV beam for the unmodified 60017 detector and the detector with a 1.6 mm airgap. Curves show errors in doses obtained from uncorrected detector readings across 0.5 × 0.5 and 1.5 × 1.5 cm^2 fields at 5 cm depth in water, relative to the on-axis dose. ± 2 s.d. confidence intervals are shown.

ratio of PDDs measured using the unmodified detector and the detector with the 1.6 mm airgap, after allowing for a 1/2 mm difference in EPOMs between the detectors (table 3). This ratio differs negligibly from one at depths ≥1 cm.

3.3. Imaging of detectors explains anomalous experimental trends

Our Monte Carlo calculations predicted that the 60017 diode detector with the 1.6 mm thick, 3.6 mm diameter airgap would perform well in small fields, and this has been confirmed by the experimental data. However, the Monte Carlo calculations also predicted that on-axis $k_{Q_{0.5,\,4\,cm}}^{0.5,\,4\,cm}$ values would rise monotonically with detector airgap thickness, but measured $k_{Q_{0.5,\,4\,cm}}^{0.5,\,4\,cm}$ values did not vary monotonically.

In figure 8(a) simulated and measured on-axis $k_{Q_{0.5,\,4\,cm}}^{0.5,\,4\,cm}$ values obtained in the 6 MV beam at 5 cm depth are plotted against airgap thickness. The two sets of results agree reasonably for detectors with 0.0, 1.0, 1.2 and 1.6 mm thick airgaps, but differ notably for the detectors with 0.6, 0.8 and 1.4 mm airgaps. In figure 8(b) experimental 6 and 15 MV $k_{Q_{0.5,\,4\,cm}}^{0.5,\,4\,cm}$ values are plotted together. Patterns of change in measured $k_{Q_{0.5,\,4\,cm}}^{0.5,\,4\,cm}$ values with airgap thickness were similar at the two energies, despite being obtained from different diode readings, film measurements and film calibration curves, indicating that the anomalous results were not caused by individual measurement errors.

While airgap thicknesses visualized in micro-CT mages of the detectors varied as expected, the imaged thickness of the dense epoxy resin overlying the silicon sensitive volume differed from one detector to another whereas in detector blueprints it was fixed. Figure 9 shows micro-CT slices of detectors with 1.4 and 1.6 mm thick airgaps, in which the epoxy layer is around 0.3 mm thinner in the detector with the 1.4 mm

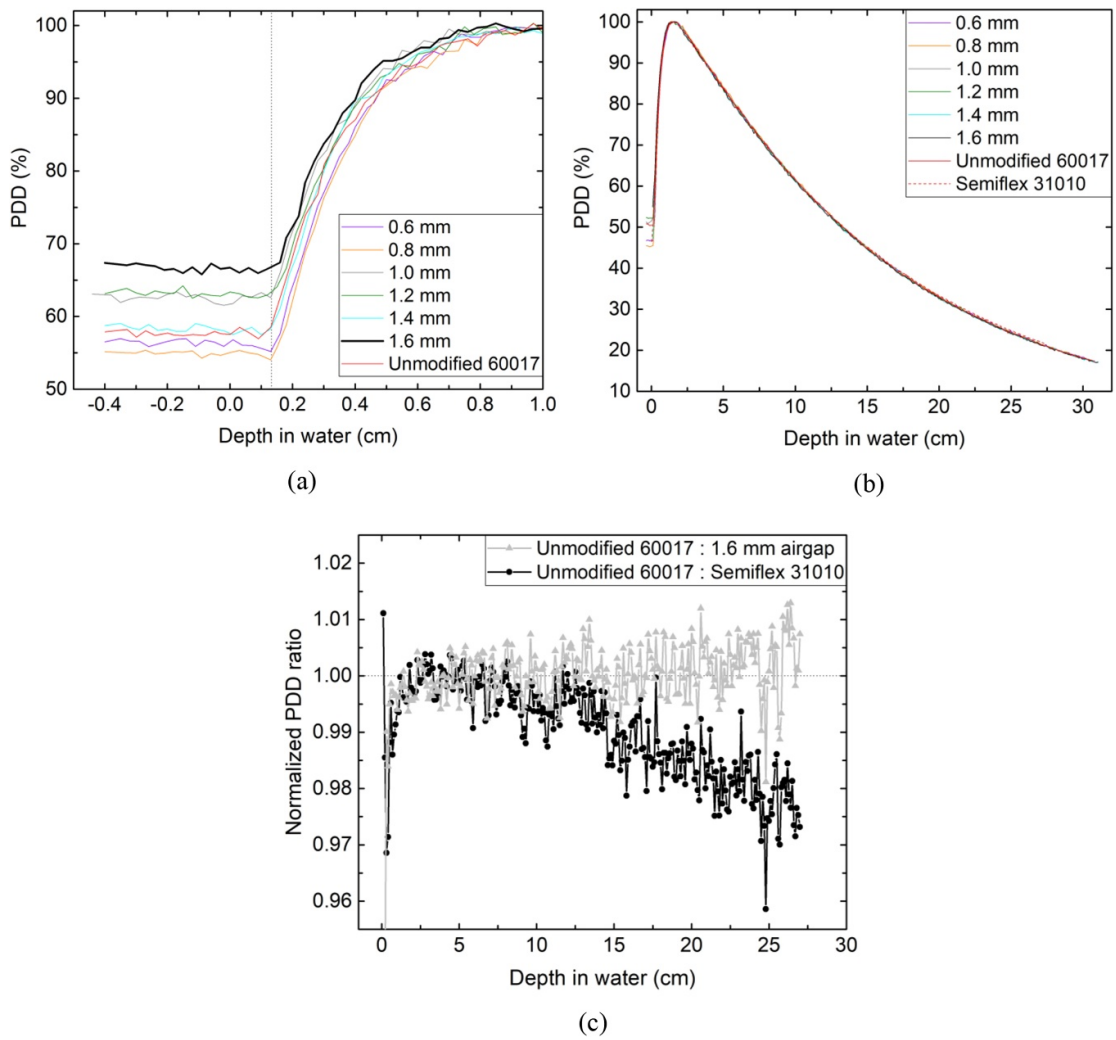

Figure 7. 6 MV depth-dose data measured experimentally using diode detectors and a Semiflex 31010 ionization chamber: (a) build-up regions of 0.5 × 0.5 cm^2 field depth-doses; (b) full 4 × 4 cm^2 field PDDs; (c) ratios of 4 × 4 cm^2 PDDs measured using different detectors, calculated after correcting for effects of small differences in measurement points due to EPOM shifts via linear interpolation, and normalized to unity at 5 cm depth.

Table 3. Experimentally measured EPOM shifts in 6 MV 0.5 × 0.5, 1.5 × 1.5 and 4 × 4 cm^2 fields for diode detectors with airgaps. Each shift describes the location of the detector EPOM relative to a point 1.33 mm below the detector's top surface, positive shifts describing deeper EPOMs.

	0.5 × 0.5 cm^2 field	1.5 × 1.5 cm^2 field	4 × 4 cm^2 field	Average
Airgap thickness(mm)		EPOM shift(mm)		
0.6	−0.3	0.0	−0.3	**−0.2**
0.8	−0.4	−0.3	−0.2	**−0.3**
1.0	0.3	0.1	0.4	**0.3**
1.2	0.0	0.0	0.1	**0.0**
1.4	0.0	−0.1	0.1	**0.0**
1.6	0.5	0.4	0.5	**0.5**

airgap. To check the influence of epoxy thickness on small field detector response, we recomputed the 6 MV $k_{Q_{0.5,\,4\,\mathrm{cm}}}^{0.5,\,4\,\mathrm{cm}}$ value on-axis at 5 cm depth in water for a modelled detector with a 1.6 mm thick airgap and an epoxy layer 0.3 mm thinner than the blueprint specification. The $k_{Q_{0.5,\,4\,\mathrm{cm}}}^{0.5,\,4\,\mathrm{cm}}$ value obtained was 1.039 ± 0.006, significantly higher than the 0.995 ± 0.006 value calculated when the epoxy thickness matched the blueprint, and demonstrating that small, within-tolerance variations in epoxy thickness can explain the experimentally observed non-monotonic variation of $k_{Q_{0.5,\,4\,\mathrm{cm}}}^{0.5,\,4\,\mathrm{cm}}$ with airgap thickness (figure 5). The difference in epoxy layer thickness will also have contributed to the $^1/_2$ mm difference between the experimentally determined EPOMs of detectors with 1.4 and 1.6 mm thick airgaps (table 3).

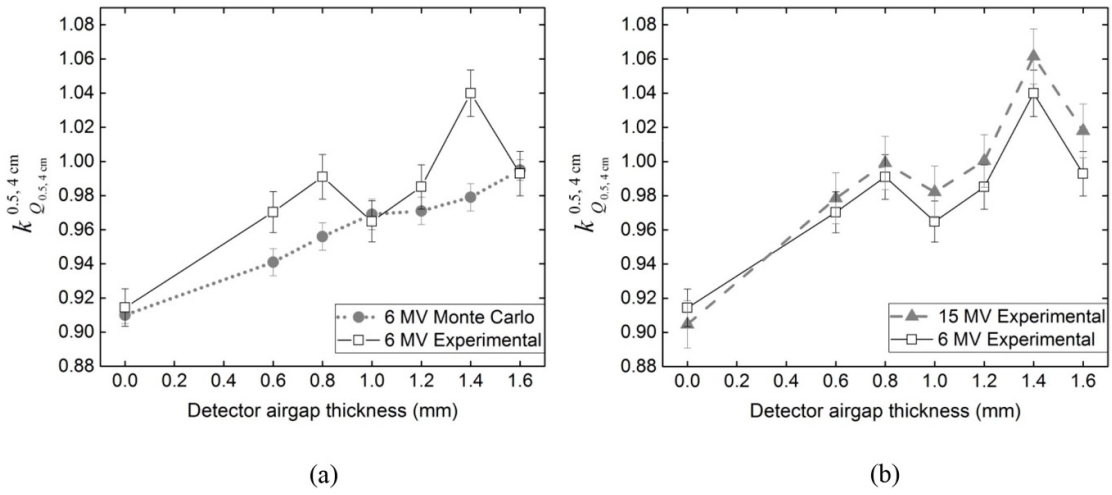

Figure 8. On-axis $k_{Q_{0.5,4\,cm}}^{0.5,4\,cm}$ correction factors for detectors at 5 cm depth in water, plotted against airgap thickness. (a) 6 MV Monte Carlo and experimentally measured factors. (b) 6 and 15 MV experimentally measured factors. ±2 s.d. confidence intervals are shown.

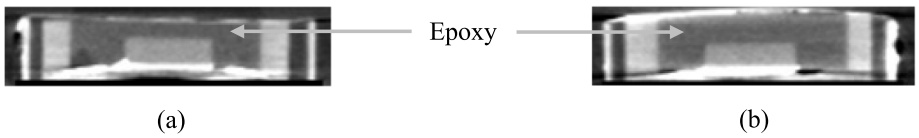

Figure 9. Micro-CT images of diode detectors with (a) 1.4 mm and (b) 1.6 mm airgaps. The central light grey structures are the silicon cuboids, and the surrounding darker grey volumes are the epoxy housings. Lower density structures are shown in black. The airgap lies above the epoxy layers, but like other detector components is largely omitted for confidentiality reasons.

4. Discussion

Our Monte Carlo calculations show that density compensation can comprehensively improve diode detectors' dosimetric performance throughout small fields. Specifically, in fields of size $\geq 0.5 \times 0.5$ cm^2, on- or off-axis at 5 or 15 cm depth in 6 or 15 MV beams, the maximum error in doses obtained from computationally simulated detector readings uncorrected by $k_{Q_{clin},Q_{msr}}^{f_{clin},f_{msr}}$ factors was 11.9% for an unmodified PTW 60017 diode detector, compared to 2.2% for a 60017 detector with a 1.6 mm thick, 3.6 mm diameter airgap added. On-axis, the largest simulated error for the modified detector was 0.6%.

The depth of the EPOM below the detector's top surface was roughly 1/2 mm greater for the 60017 diode with the airgap added. But after accounting for the change in EPOM, Monte Carlo simulations of the depth-dose curves that would be measured by the unmodified and modified detectors differed negligibly. The increased EPOM depth due to the airgap appears at odds with an observation of Underwood *et al* (2015b) that the addition of a relatively thin airgap 'does not perceptibly offset the instrument's EPOM'. However, close examination of the data presented in figure 6(b) of Underwood *et al* shows that a 1 mm airgap changed the EPOM by around 0.3 mm, in line with the roughly 0.5 mm EPOM change computed here for a 1.6 mm thick airgap. Overall, then, the computational data consistently show that airgaps increase the EPOM depth, but only by around one-third of the airgap thickness.

These computational results have been validated by our experimental measurements. In 6 and 15 MV 0.5×0.5 cm^2 fields, on- and off-axis at 5 and 15 cm depths, the maximum errors in doses obtained experimentally from the uncorrected readings of an unmodified 60017 diode and a detector with a 1.6 mm airgap added were respectively 11.7% (15 MV, −0.3 mm off-axis, 5 cm depth) and 4.1% (15 MV, + 0.4 mm off-axis, 15 cm depth), the latter result possibly overestimating the underlying detector inaccuracy due to noisy film measurements. The experimental data also indicated a 1/2 mm shift in EPOM for the detector with the 1.6 mm airgap compared to the unmodified detector, the measured shift being the same in 0.5×0.5 and 4×4 cm^2 fields (table 3).

The 1.6 mm optimal airgap thickness found here for 3.6 mm diameter airgaps is greater than the 1 mm optimal thickness determined by Underwood *et al* (2015b). This is largely because the airgaps studied by Underwood *et al* were wider than 3.6 mm, and consequently could be thinner while achieving the same level

of density compensation (table 1). Additionally, a 4 × 4 cm^2 reference field was used here rather than the 10 × 10 cm^2 field used by Underwood *et al*, and for all the diodes tested there was a roughly 1% difference between response in 4 × 4 and 10 × 10 cm^2 fields (figure 5) due to spectral effects. For an unmodified 60017 detector, $k_{Q_{0.5,\,10\,cm}}^{0.5,\,10\,cm}$ is consequently slightly larger than $k_{Q_{0.5,\,4\,cm}}^{0.5,\,4\,cm}$, and therefore a $k_{Q_{0.5,\,10\,cm}}^{0.5,\,10\,cm}$ value of one can be achieved using slightly less air compensation than is required for $k_{Q_{0.5,\,4\,cm}}^{0.5,\,4\,cm}$ to reach unity.

In the 6 MV beam, Monte Carlo calculated $k_{Q_{0.5,\,4\,cm}}^{0.5,\,4\,cm}$ values did not quite reach one at 5 or 15 cm depths even for a 1.6 mm thick airgap, although in the 15 MV beam $k_{Q_{0.5,\,4\,cm}}^{0.5,\,4\,cm}$ values were a little greater than one for this airgap thickness. To check whether detector performance could be improved further by adding a thicker airgap, we carried out additional Monte Carlo calculations to determine the 6 MV $k_{Q_{0.5,\,4\,cm}}^{0.5,\,4\,cm}$ factor at 5 cm depth in water for a detector with a 1.8 mm thick airgap. The 1.009 ± 0.006 value of $k_{Q_{0.5,\,4\,cm}}^{0.5,\,4\,cm}$ obtained for this modified detector shows that the 60017 diode is over-compensated by airgaps much thicker than 1.6 mm.

Experimentally, a 2% drop in the response of diode detectors relative to an ionization chamber was seen between depths of 5 and 27 cm (figure 7), but this was not reflected in Monte Carlo calculations of diode-measured and in-water PDDs. The decrease seen experimentally is likely related to a dose-rate dependence of 60017 diode readings, and may explain why measured $k_{Q_{0.5,\,4\,cm}}^{0.5,\,4\,cm}$ values were 1%–2% higher at a measurement depth of 15 cm than at 5 cm (figure 5), whereas there was little difference between Monte Carlo calculated $k_{Q_{0.5,\,4\,cm}}^{0.5,\,4\,cm}$ values at the two depths (table 2).

For the unmodified detector we obtained $k_{Q_{0.5,\,4\,cm}}^{0.5,\,4\,cm}$ values of 0.91–0.93 at 5 and 15 cm depths in water, with good agreement between computational and experimental results. This agreement in part reflects the accuracy of the jaw calibration on the TrueBeam linac used for the measurements: at 100 cm SSD and a measurement depth of 5 cm, the nominal 5 and 7 mm wide fields set would be expected to have full-width-half-maximum values of 5.25 and 7.35 mm, and film measurements put the physically-realized widths at 5.18 and 7.09 mm. Other studies have reported $k_{Q_{0.5,\,4\,cm}}^{0.5,\,4\,cm}$ values of around 0.94 for this detector (IAEA 2017), and the lower values obtained here reflect our use of jaw-defined rather than multileaf-defined fields: for a 10 MV beam Underwood *et al* (2015a) measured $k_{Q_{0.5,\,10\,cm}}^{0.5,\,10\,cm}$ factors for fields defined by jaws and the multileaf of a TrueBeam linac, and found that the factor was roughly 3% higher for the jaw-defined fields.

Our experimental results did not demonstrate the progressive rise in $k_{Q_{0.5,\,4\,cm}}^{0.5,\,4\,cm}$ values with increasing detector airgap thickness seen in the Monte Carlo data. The anomalous, non-monotonic pattern obtained experimentally was not due to measurement errors, nor to manufacturing errors in the thickness of airgaps, but is explained by variations from one detector to another in the thickness of epoxy resin overlying the detector sensitive volume, the variations reflecting the tolerance set in the detector manufacturing process.

Previous Monte Carlo investigations have noted that detector response in small fields is influenced by component densities in general, not just the density of the sensitive volume (Cranmer-Sargison *et al* 2012, Underwood *et al* 2013a). Indeed, one study reported that the response of diode detectors in small fields varied with the epoxy resin density (Francescon *et al* 2012), and so it is unsurprising that the response of detectors in small fields also depends on the thickness of this relatively dense material. A corollary is that fine-tuning a detector's small field response using an airgap engineered to a tenth of a millimeter will work reproducibly only if comparable manufacturing tolerances can be placed on the dimensions of dense components.

Recently PTW-Freiburg began marketing a new 60023-type diode detector (Schönfeld *et al* 2019) in which the silicon lattice has been adjusted to minimize dose-rate effects. Reflecting the findings described here, other detector components have been modified to have densities closer to that of water, thus limiting detector-to-detector variations in small field response that would otherwise result from finite geometrical tolerances of the manufacturing process. In a future article we will describe the utility of density compensating the 60023 detector.

5. Conclusions

Density compensation can improve the dosimetric performance of diode detectors in small fields over a wide range of photon beam energies, field-sizes, depths in water and distances off-axis. For a PTW 60017 diode detector modified to include a 1.6 mm thick, 3.6 mm diameter airgap, maximum errors of 2.2% and 4.1% were determined computationally and experimentally for doses obtained from detector readings uncorrected by $k_{Q_{clin},Q_{msr}}^{f_{clin},f_{msr}}$ factors in 6 or 15 MV beams, on- or off-axis, at 5 or 15 cm depths in fields as small as 0.5 × 0.5 cm^2. These values were much lower than the 11.9% and 11.7% maximum errors determined computationally and experimentally for an unmodified 60017 detector.

For some detectors, simulated and measured responses differed in 0.5 × 0.5 cm^2 fields. This was a consequence of the finite manufacturing tolerance on the thickness of a relatively dense layer of epoxy resin. For density compensation to perform well with good detector-to-detector reproducibly, tolerances on dense detector component dimensions should lie below the scale on which they notably affect detector response in

small fields (<0.3 mm for the epoxy layer thickness), or components should be modified to have more water-like densities.

Acknowledgments

The authors thank PTW-Freiburg for manufacturing and providing the diode detectors tested in this work. Medical Research Council funding (MC_PC_12004) for the CRUK/MRC Oxford Institute for Radiation Oncology is gratefully acknowledged.

Conflicts of interest

Dr Jan U Würfel is an employee of PTW-Freiburg. The other authors have no conflicts of interest.

References

Alfonso R *et al* 2008 A new formalism for reference dosimetry of small and nonstandard fields *Med. Phys.* **35** 5179–86

Bassinet C *et al* 2013 Small fields output factors measurements and correction factors determination for several detectors for a Cyberknife® and linear accelerators equipped with microMLC and circular cones *Med. Phys.* **40** 071725

Berger M J, Hubbell J H, Seltzer S M, Chang J, Coursey J S, Sukumar R, Zucker D S and Olsen K 2010 *XCOM: Photon Cross Section Database (Version 1.5) Technical Report* (Gaithersburg, MD: National Institute of Standards and Technology)

Charles P H, Cranmer-Sargison G, Thwaites D I, Kairn T, Crowe S B, Pedrazzini G, Aland T, Kenny J, Langton C M and Trapp J V 2014 Design and experimental testing of air slab caps which convert commercial electron diodes into dual purpose, correction-free diodes for small field dosimetry *Med. Phys.* **41** 101701

Charles P H, Crowe S B, Kairn T, Knight R T, Hill B, Kenny J, Langton C M and Trapp J V 2013 Monte Carlo-based diode design for correction-less small field dosimetry *Phys. Med. Biol.* **58** 4501–12

Cranmer-Sargison G, Weston S, Evans J A, Sidhu N P and Thwaites D I 2012 Monte Carlo modelling of diode detectors for small field MV photon dosimetry: detector model simplification and the sensitivity of correction factors to source parameterization *Phys. Med. Biol.* **57** 5141–5153

Fenwick J D, Georgiou G, Rowbottom C G, Underwood T S A, Kumar S and Nahum A E 2018 Origins of the changing detector response in small megavoltage photon radiation fields *Phys. Med. Biol.* **63** 125003–125015

Francescon P, Beddar S, Satariano N and Das I J 2014 Variation of for the small-field dosimetric parameters percentage depth dose, tissue-maximum ratio, and off-axis ratio *Med. Phys.* **41** 101708

Francescon P, Kilby W, Satariano N and Cora S 2012 Monte Carlo simulated correction factors for machine specific reference field dose calibration and output factor measurement using fixed and iris collimators on the CyberKnife system *Phys. Med. Biol.* **57** 3741–58

Hartmann G H and Zink K 2018 Decomposition of the dose conversion factor based on fluence spectra of secondary charged particles: application to lateral dose profiles in photon fields *Med. Phys.* **45** 4246–56

Hubbell J H and Seltzer S M 2004 *Tables of X-Ray Mass Attenuation Coefficients and Mass Energy-Absorption Coefficients (Version 1.4)* (Gaithersburg, MD: National Institute of Standards and Technology)

IAEA 2017 *Dosimetry of Small Static Fields Used in Radiotherapy: An International Code of Practice for Reference and Relative Dose Determination Technical Report Series 484* (Vienna: International Atomic Energy Agency)

Jursinic P A 2013 Dependence of diode sensitivity on the pulse rate of delivered radiation *Med. Phys.* **40** 0217201–09

Kawrakow I, Mainegra-Hing E and Rogers D W O 2006 EGSnrcMP: The Multi-Platform Environment for EGSnrc *NRCC Report PIRS-877* (Ottawa: National Research Council of Canada)

Kawrakow I, Mainegra-Hing E, Rogers D W O, Tessier F and Walters B R B 2011 The EGSnrc code system: Monte Carlo simulation of electron and photon transport *NRCC Report PIRS-701* (Ottawa: National Research Council of Canada)

Lewis D, Micke A, Yu X and Chan M F 2012 An efficient protocol for radiochromic film dosimetry combining calibration and measurement in a single scan *Med. Phys.* **39** 6339–50

Micke A, Lewis D F and Yu X 2011 Multichannel film dosimetry with nonuniformity correction *Med. Phys.* **38** 2523–34

Morales J, Butson M, Crowe S B, Hill R and Trapp J V 2016 An experimental extrapolation technique using the Gafchromic EBT3 film for relative output factor measurements in small x-ray fields *Med. Phys.* **43** 4687–92

National Institute of Science and Technology 2018 *Stopping Power and Range Tables for Electrons* (https://physics.nist.gov/cgi-bin/Star/e_table.pl) (Accessed: 15 September 2018)

Papaconstadopoulos P, Hegyi G, Seuntjens J and Devic S 2014 A protocol for EBT3 radiochromic film dosimetry using reflection scanning *Med. Phys.* **41** 6pp

PTW 2018 *Ionizing Radiation Detectors, Including Codes of Practice* (Freiburg: PTW)

Rogers D W O, Kawrakow I, Seuntjens J P, Walters B R B and Mainegra-Hing E 2011b *NRCC Report No. PIRS 702 Rev C: NRC User Codes for EGSnrc* (Ottawa: National Research Council of Canada)

Rogers D W O, Walters B and Kawrakow I 2011a *NRCC Report No. 0509 (A) Rev L; BEAMnrc User's Manual* (Ottawa: National Research Council of Canada)

Schönfeld A-B, Poppinga D, Kranzer R, Dewilde R L, Willborn K, Poppe B and Looe H K 2019 Technical note: characterization of the new microSilicon diode detector *Med. Phys.* **46** 4257–62

Scott A J D, Kumar S, Nahum A E and Fenwick J D 2012 Characterizing the influence of detector density on dosimeter response in non-equilibrium small photon fields *Phys. Med. Biol.* **57** 4461–76

Scott A J D, Nahum A E and Fenwick J D 2008 Using a Monte Carlo model to predict dosimetric properties of small radiotherapy photon fields *Med. Phys.* **35** 4671–84

Underwood T S A, Rowland B C, Ferrand R and Viellevigne L 2015a Application of the Exradin W1 scintillator to determine Ediode 60017 and microdiamond 60019 correction factors for relative dosimetry within small MV and FFF fields *Phys. Med. Biol.* **60** 6669–83

Underwood T S A, Thompson J, Bird L, Scott A J D, Patmore P, Winter H C, Hill M A and Fenwick J D 2015b Validation of a prototype DiodeAir for small field dosimetry *Phys. Med. Biol.* **60** 2939–53

Underwood T S A, Winter H C, Fenwick J D and Hill M A 2012 OC-0512 Modifying detector designs for small field dosimetry *Radiother. Oncol.* **103** S206

Underwood T S A, Winter H C, Hill M A and Fenwick J D 2013a Detector density and small field dosimetry: integral versus point dose measurement schemes *Med. Phys.* **40** 16pp

Underwood T S A, Winter H C, Hill M A and Fenwick J D 2013b Mass-density compensation can improve the performance of a range of different detectors under non-equilibrium conditions *Phys. Med. Biol.* **58** 8295–310

Wulff J, Zink K and Kawrakow I 2008 Efficiency improvements for ion chamber calculations in high energy photon beams *Med. Phys.* **35** 1328–36